Electronic Supplementary Material (ESI) for Physical Chemistry Chemical Physics.

Supporting information for: Revisiting the Volmer-Heyrovský mechanism of hydrogen evolution on a nitrogen doped carbon nanotube: Constrained molecular dynamics *versus* the nudged elastic band method

Rasmus Kronberg, Heikki Lappalainen, and Kari Laasonen*

Research Group of Computational Chemistry, Department of Chemistry and Materials Science, Aalto University, P.O. Box 16100, FI-00076 Aalto, Finland

E-mail: kari.laasonen@aalto.fi

CI-NEB electrode potential and surface charges

The electrode potential dependence of the CI-NEB energy profiles were estimated using the Chan-Nørskov charge-extrapolation scheme[1,2]. Since each CI-NEB image along the optimized reaction path corresponds to a different governing electrode potential and surface charge due to fractional charge transfer, constant electrode potential profiles are derived in practice by referencing each CI-NEB image to a single chosen reference state (*e.g.* the 3rd CI-NEB image) in accordance with Equation (8) in the main text. The electrode potential at this reference state sets the constant electrode potential for the corrected "grand canonical" energy profile. Performing this procedure using every single CI-NEB image as a reference state in turn with each state corresponding to a different electrode potential (and surface charge), a set of constant potential energy profiles with as many members as there are images in the CI-NEB calculation is obtained. Shifting each energy profile finally such that the energy of the initial state is at 0 eV yields the constant electrode potential energy profiles reported in the main text.

Electrode potentials *vs.* SHE and surface charges (Hirshfeld) were calculated for each CI-NEB image of the Volmer (Figure S1) and Heyrovský (Figure S2) reactions. In the case of the Volmer reaction, the surface charge was calculated by considering all carbon atoms as well as the nitrogen dopant, while for the Heyrovský reaction also the adsorbed H* intermediate was included up until the transition state at which the atom is no longer considered to reside on the surface. For both cases, the results illustrate a monotonously increasing electrode potential and surface charge, as expected based on the canonical nature of Kohn-Sham DFT. The steepest increase in both quantities is observed close to the transition state, NEB images 6 and 5, respectively. Furthermore, a closely linear correspondence between the electrode potential and the surface charge is observed from Figures S1c and S2c, in accordance with the Gouy-Chapman model of the electrochemical double layer at small potentials. It is noteworthy that the hybrid PBE0 functional yields electrode potentials that are consistently positively shifted by roughly 0.3-0.4 eV with respect to PBE. The slope in Figures S1c and

S2c can be used to estimate the differential capacitance of the NCNT according to

$$C = \frac{d\sigma}{dU} = \frac{1}{\Sigma}\frac{dq}{dU}, \tag{S1}$$

where σ is the surface charge density, q the surface charge, Σ is the model NCNT surface area (*ca.* 440 Å^2) and U is the electrode potential. This yields the approximate value $2 \pm 1\,\mu\mathrm{F\,cm^{-2}}$, which increases to $3 \pm 1\,\mu\mathrm{F\,cm^{-2}}$ upon hydrogen adsorption. The error margin corresponds to the standard error of the fit. The capacitance estimates are of the same order of magnitude as previous experimental estimates for pristine CNTs in dilute electrolyte[3].

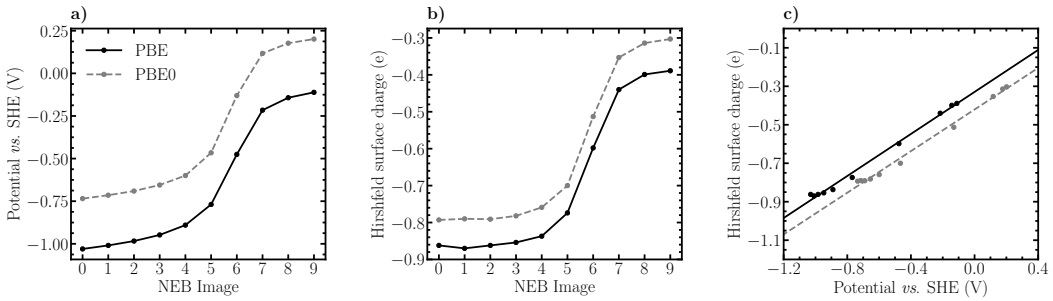

Figure S1: a) Electrode potential *vs.* SHE and b) Hirshfeld surface charges as determined from the CI-NEB configurations of the Volmer reaction. The change in electrode potential as a function of the surface charge is illustrated in c). Note that the legend in a) refers to all panels.

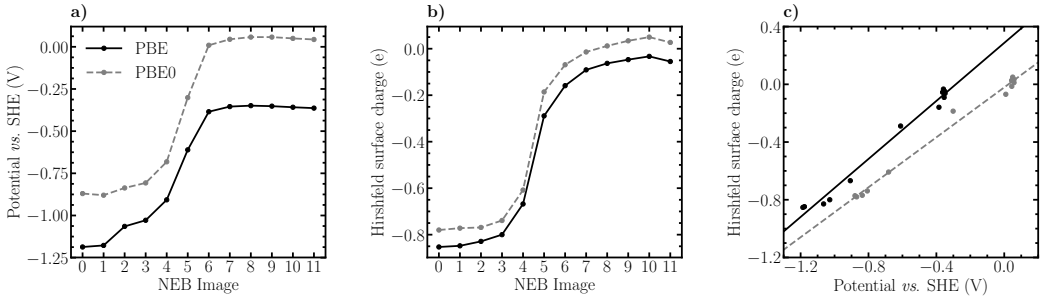

Figure S2: a) Electrode potential *vs.* SHE and b) Hirshfeld surface charges as determined from the CI-NEB configurations of the Heyrovský reaction. The change in electrode potential as a function of the surface charge is illustrated in c). Note that the legend in a) refers to all panels.

Constrained MD simulations – Forces and errors

The time evolution of the Lagrange multiplier (force of constraint) of the Volmer and Heyrovský initial (IS), transition (TS) and final states (FS) are shown in Figures S3a and S4a as examples. The first 2 ps of the simulations have been excluded (equilibration) and the remainder of the trajectories can be seen to exhibit rather constant fluctuations without long range drift. This is also illustrated by the plotted cumulative averages, which reach a relatively constant value within a window of 2-3 ps from the start of the production part of the simulations. As illustrated in the rightmost panels, the obtained forces sample a normal distribution very closely with mean values $\lesssim 0.1\,\mathrm{eV\,\AA^{-1}}$. Ideally, the force at the initial, transition and final states should be zero.

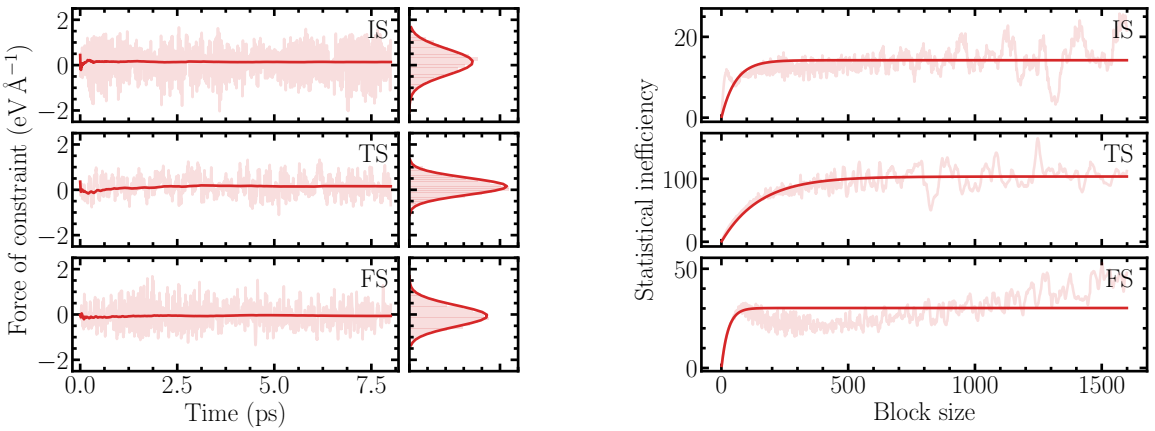

(a) (b)

Figure S3: a) Time evolution of the force of constraint (Lagrange multiplier) of the initial (IS), transition (TS) and final states (FS) of the Volmer reaction. The cumulative mean force is indicated by the red curve. b) Calculation of the statistical inefficiency corresponding to the force of constraint (Lagrange multiplier) of the initial, transition and final state trajectories of the Volmer reaction. An asymptotic fit has been added to estimate the limit at which successive block averages become uncorrelated.

To calculate error margins for the sampled forces of constraint we have applied the block averaging method[4] in conjunction with the statistical inefficiency test[5] to appropriately account for correlation within the data. Briefly, the data Lagrange multiplier vs. MD step

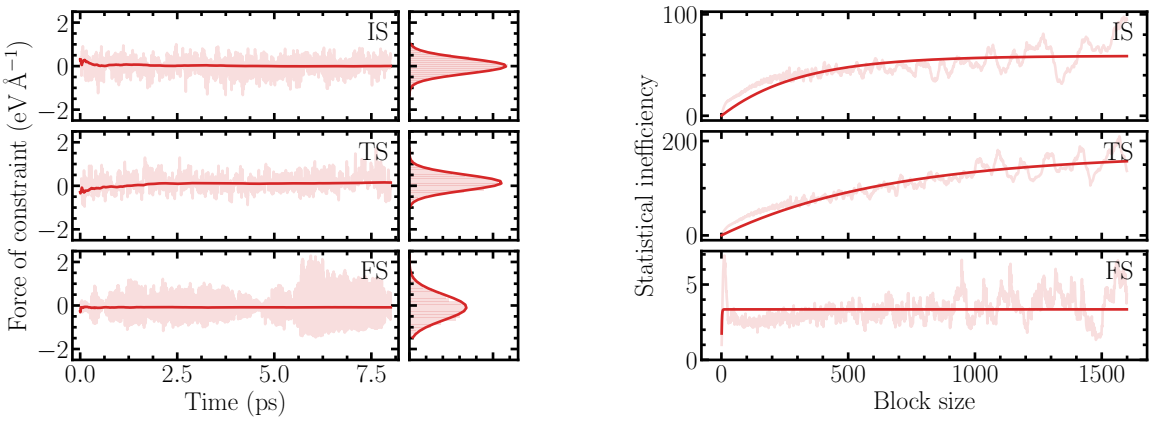

Figure S4: a) Time evolution of the force of constraint (Lagrange multiplier) of the initial, transition and final states of the Heyrovský reaction. The cumulative mean force is indicated by the red curve. b) Calculation of the statistical inefficiency corresponding to the force of constraint (Lagrange multiplier) of the initial, transition and final state trajectories of the Heyrovský reaction. An asymptotic fit has been added to estimate the limit at which successive block averages become uncorrelated.

number is split into blocks of size τ_b and the block average of each segment is calculate to form a new dataset. This is done for increasing block sizes (up to a tenth of the full simulation) to obtain several block averaged datasets. Denoting the bias-corrected sample variances of the whole simulation and the block averaged ensemble by $\sigma^2(\lambda)$ and $\sigma^2(\langle\lambda\rangle_b)$, respectively, the statistical inefficiency is defined by

$$s = \lim_{\tau_b \to \infty} \frac{\tau_b \sigma^2(\langle\lambda\rangle_b)}{\sigma^2(\lambda)} \tag{S2}$$

In practice, we fit an asymptotic function of the form $f(\tau_b) = a\left(1 - e^{-b\tau_b}\right)$ to the data and estimate the limit as $s \approx \lim_{\tau_b \to \infty} f(\tau_b) = a$. At the limit, successive block averaged datasets are (approximately) statistically uncorrelated, allowing the estimation of the proper variance of the mean as

$$\sigma^2(\langle\lambda\rangle) = \frac{s\sigma^2(\lambda)}{\tau}, \tag{S3}$$

where τ is the length of the full simulation. The statistical inefficiency including asymptotic fits are demonstrated for the Volmer and Heyrovský initial, transition and final states in Figures S3b and S4b.

The uncertainty in the obtained free energy profiles was calculated using the determined variances, including the effect of error propagation upon thermodynamic integration. Employing the cumulative (composite) trapezoidal method, the integral can be written as

$$\begin{aligned}\Delta A(\xi) &= -\int_{\xi_0}^{\xi} d\xi \left\langle \lambda(\xi) \right\rangle_{\xi} \approx -\sum_{k=1}^{N} \frac{\left\langle \lambda(\xi_{k-1}) \right\rangle_{\xi_{k-1}} + \left\langle \lambda(\xi_k) \right\rangle_{\xi_k}}{2} \Delta\xi_k \\ &= -\frac{\Delta\xi_1}{2} \left\langle \lambda(\xi_0) \right\rangle_{\xi_0} - \frac{(\Delta\xi_1 + \Delta\xi_2)}{2} \left\langle \lambda(\xi_1) \right\rangle_{\xi_1} - \dots \\ &\dots - \frac{(\Delta\xi_{N-1} + \Delta\xi_N)}{2} \left\langle \lambda(\xi_{N-1}) \right\rangle_{\xi_{N-1}} - \frac{\Delta\xi_N}{2} \left\langle \lambda(\xi_N) \right\rangle_{\xi_N}\end{aligned} \tag{S4}$$

where $\Delta\xi_k = \xi_k - \xi_{k-1}$. Since the calculated variances $\sigma^2(\langle\lambda(\xi)\rangle_{\xi})$ have been appropriately decorrelated (zero covariance), the variance of the mean free energy at a given ξ is obtained using the total differential as

$$\begin{aligned}\sigma^2(\Delta A(\xi)) &= \sum_{i=0}^{N} \left(\frac{\partial \Delta A(\xi)}{\partial \left\langle \lambda(\xi_i) \right\rangle_{\xi_i}} \right)^2 \sigma^2(\langle\lambda(\xi_i)\rangle_{\xi_i}) \\ &= \frac{(\Delta\xi_1)^2}{4}\sigma^2(\langle\lambda(\xi_0)\rangle_{\xi_0}) + \frac{(\Delta\xi_1 + \Delta\xi_2)^2}{4}\sigma^2(\langle\lambda(\xi_1)\rangle_{\xi_1}) + \dots \\ &\dots + \frac{(\Delta\xi_{N-1} + \Delta\xi_N)^2}{4}\sigma^2(\langle\lambda(\xi_{N-1})\rangle_{\xi_{N-1}}) + \frac{(\Delta\xi_N)^2}{4}\sigma^2(\langle\lambda(\xi_N)\rangle_{\xi_N}).\end{aligned} \tag{S5}$$

Finally, the obtained variances of the mean free energy were used to compute error limits corresponding to the 95 % confidence intervals by taking the square root of the variance to get the standard error of the mean and subsequently multiplying by 1.96.

Grotthuss mechanism

To illustrate the initiation of the Grotthuss proton shuttling mechanism in the constrained MD simulations (unrestrained ensemble), the time evolution of the O–H′ distances of the Volmer and Heyrovský reactions are plotted in Figure S5 for the transition state and two immediately following trajectories. Please see the main text for the definition of the atomic labels.

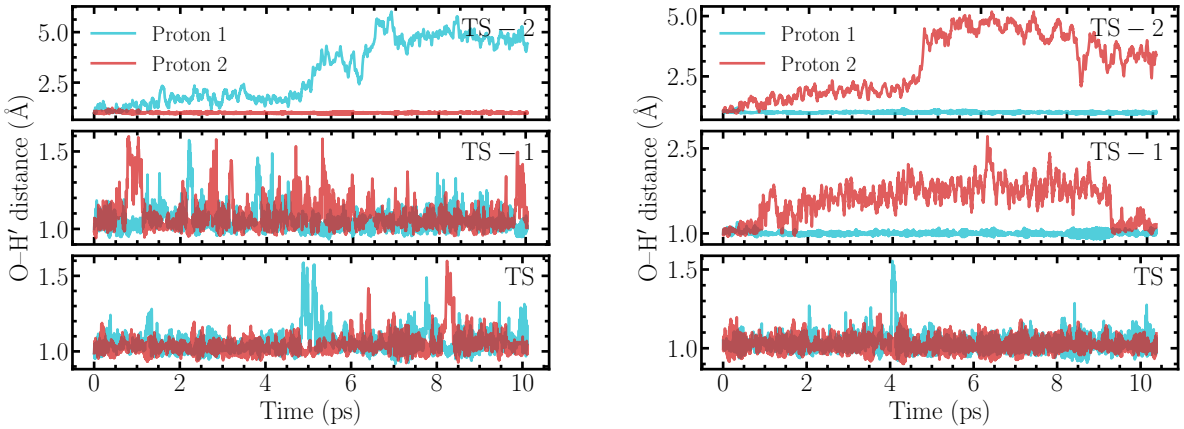

Figure S5: a) Time evolution of the O–H′ distances of the a) Volmer and b) Heyrovský reactions at the transition state (TS) and two following states. Specifically, TS − 1 refers to the state just before the TS on the reactant side of the reaction (solvated proton) and TS − 2 to the state just before this one. The values of the reaction coordinate constraints are 0.3 Å, 0.4 Å and 0.6 Å for the TS, TS − 1 and TS − 2 states of the Volmer reaction, respectively, while for the Heyrovský reaction the values are −1.8 Å, −1.6 Å and −1.4 Å, respectively.

For both the Volmer and Heyrovský reactions we observe that the H′ protons bound to the donating oxygen, but not participating in the Volmer and Heyrovský reactions, are very stable at the transition state. Indeed, the protons remain strongly bound to the oxygen atom and only very brief fluctuations are seen where either of the protons transfer closer to the neighboring O′ atoms (distance increases from *ca.* 1.0 Å to 1.5 Å). However, in the following TS − 1 trajectories the proton hopping between O and O′ intensifies in the simulation of the Volmer reaction, while a more stationary transfer to the H′ atom is seen for the Heyrovský

reaction. The O′ atom including the hydrogens stay nevertheless close to the O atom, which is evidenced by the fact that the transferred H′ is observed to return to the O atom at the end of the trajectory. Finally, in the TS − 2 trajectories the protons transferring to the NCNT in the Volmer reaction or forming H_2 in the Heyrovský reaction are so far from the surface that the Grotthuss mechanism becomes energetically facile. This is seen as a fast transfer of either of the H′ protons to either of the O′ oxygens, followed by successive proton transfers and water diffusion. This is observed in the upper panels of Figure S5 as a gradual increase in the O-H′ distance from 1.0 Å to more than 5.0 Å during the course of the simulations. Simultaneously, the intermediate $H_7O_3{}^+$ proton complexes identified at the TS and TS − 1 states decay and the excess proton, now farther from the surface, is seen to adopt an Eigen-like configuration.

Constrained MD electrode potential and surface charges

The electrode potentials *vs.* SHE and the Hirshfeld surface charges were computed every 100 fs for each constrained MD trajectory and are illustrated in Figures S6 and S7. Strong fluctuations in the orientation of interfacial water molecules are observed to induce substantial fluctuations in the electrode potential on the order of 0.5-1.0 V, as has been previously reported[6]. Although a weak positive linear trend in the electrode potential as a function of the reaction coordinate appears to exist, the fluctuating surface dipole results in slow equilibration of the electrode potential, preventing the use of the charge-extrapolation scheme[1,2] employed for the static CI-NEB simulations. Indeed, in the case of the dynamic simulations, the electrostatic contribution to the energy change along a reaction path is not purely capacitive, but also dependent on changes in the interfacial dipole. Of course, in a sufficiently long simulation the electrode potential would equilibrate properly and if the simulation would further be of grand canonical nature (constant electrode potential, electrons exchanged with a fictitious potentiostat) the potential would be expected to remain constant across the whole reaction path. Consequently, one would also expect small long-range solvent

reorganization, with the exception of the water molecules closest to the reactive species. While such a simulation would correspond to a truly realistic electrochemical system, the practical, efficient implementation of grand canonical DFT is highly non-trivial and beyond the scope of the present work.

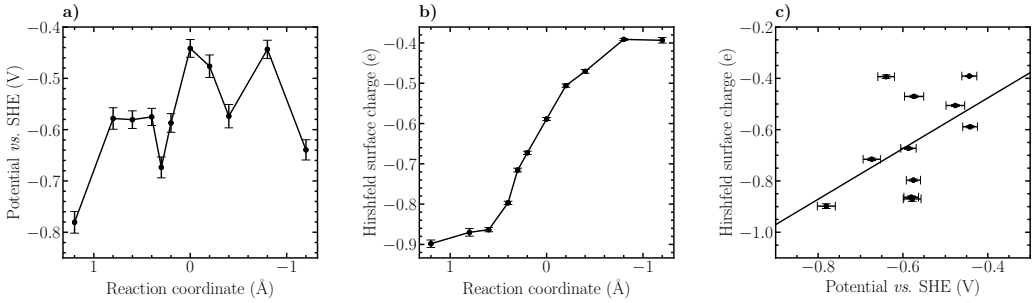

Figure S6: a) Electrode potential *vs.* SHE and b) Hirshfeld surface charges as determined from constrained MD simulations of the Volmer reaction. The change in electrode potential as a function of the surface charge is illustrated in c). The error bars indicate the standard errors of the potential and surface charge, respectively.

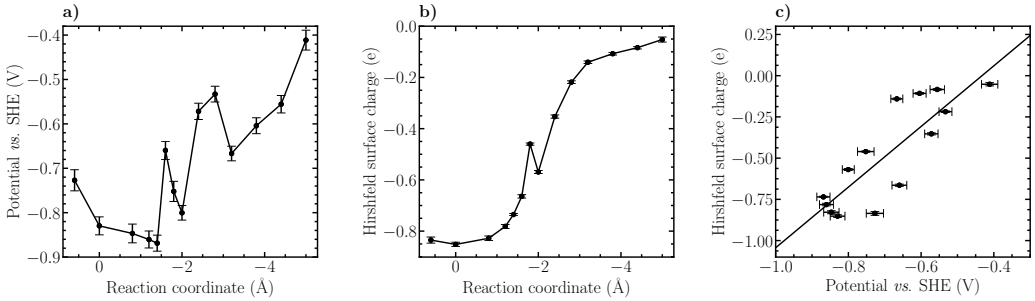

Figure S7: a) Electrode potential *vs.* SHE and b) Hirshfeld surface charges as determined from constrained MD simulations of the Heyrovský reaction. The change in electrode potential as a function of the surface charge is illustrated in c). The error bars indicate the standard errors of the potential and surface charge, respectively.

The change in the averaged surface charge along the reaction paths is, on the other hand, well equilibrated and exhibits very similar behavior as in the CI-NEB calculations. Plotting the electrode potential *vs.* the surface charge in Figures S6c and S7c allows again for an estimation of the differential capacitance. The obtained estimate is $4 \pm 2\,\mu\mathrm{F\,cm^{-2}}$ which increases to $7 \pm 2\,\mu\mathrm{F\,cm^{-2}}$ upon hydrogen adsorption. The error margin corresponds to the standard error of the fit. Although the errors are larger than for the static calculations due

to potential fluctuations, the results are qualitatively similar and agree again roughly with the previous experimental estimate for pristine CNTs[3] ($< 10\,\mu F\,cm^{-2}$ in a dilute electrolyte).

References

(1) Chan, K.; Nørskov, J. K. Electrochemical barriers made simple. *J. Phys. Chem. Lett.* **2015**, *6*, 2663–2668.

(2) Chan, K.; Nørskov, J. K. Potential dependence of electrochemical barriers from ab initio calculations. *J. Phys. Chem. Lett.* **2016**, *7*, 1686–1690.

(3) Hoefer, M.; Bandaru, P. R. Determination and enhancement of the capacitance contributions in carbon nanotube based electrode systems. *Appl. Phys. Lett.* **2009**, *95*, 183108.

(4) Flyvbjerg, H.; Petersen, H. G. Error estimates on averages of correlated data. *J. Chem. Phys.* **1989**, *91*, 461–466.

(5) Friedberg, R.; Cameron, J. E. Test of the Monte Carlo method: fast simulation of a small Ising lattice. *J. Chem. Phys.* **1970**, *52*, 6049–6058.

(6) Holmberg, N.; Laasonen, K. Ab initio electrochemistry: Exploring the hydrogen evolution reaction on carbon nanotubes. *J. Phys. Chem. C* **2015**, *119*, 16166–16178.